

Eksploatacja i Niezawodnosc - Maintenance and Reliability

Volume 29 (2027), Issue 3

https://ein.org.pl

The Polish Maintenance Society

ARCCgram: a novel blind feature extraction method for the fault diagnosis of rolling bearings

Tao Liu[1], Tao Zhang[1,*], Hong Wang[1], Yong He[1], Jian Yong Li[2]

[1] School of Mechanical Engineering, Lanzhou Jiaotong University, China
[2] School of Railway Tracks and Transportation, Wuyi University, China
* Corresponding Author: zhangtao0209404@163.com

Received: 12 July 2026
Revised: 17 October 2026
Accepted: 30 October 2026
Online: 23 November 2026

This is an open access article under the CC BY 4.0 license

Abstract

Optimal frequency band selection remains a challenging prerequisite for effective envelope analysis in rolling bearing diagnostics. Existing blind methods are prone to band-selection bias when subjected to multi-source cyclostationary interference, while target-informed methods are constrained by the requirement for precise a priori knowledge of fault characteristic frequencies (FCFs). To bridge this gap, a novel blind feature extraction method, named the adaptive ratio of cyclic content gram (ARCCgram), is proposed. By automatically capturing candidate fault frequencies (CFFs) via local maximum detection on the fast spectral coherence (SCoh) map, a novel indicator, namely adaptive ratio of cyclic content (ARCC), is formulated. This indicator evaluates candidate sub-bands within a 1/3-binary-tree filter bank by quantifying the energy proportion within CFF-centered tolerance windows, thereby successfully endowing the blind approach with cyclic frequency selectivity. Subsequently, an improved envelope spectrum is constructed via in-band spectral coherence integration to robustly identify fault signatures. Comparisons using three experimental bearing fault datasets and a simulation show that ARCCgram produces clearly identifiable spectral structures associated with the faults in the analysed records.

Keywords: *spectral coherence, optimal frequency band selection, adaptive ratio of cyclic content, rolling bearing fault diagnosis*

Article citation:
Liu T, Zhang T, Wang H, He Y, Li JY, ARCCgram: a novel blind feature extraction method for the fault diagnosis of rolling bearings, Eksploatacja i Niezawodnosc – Maintenance and Reliability 2027: 29(3) http://doi.org/10.17531/ein/242349

Highlights

- A novel blind feature extraction method, namely ARCCgram, is proposed for the fault diagnosis of rolling bearings.
- A novel indicator, named ARCC, is proposed to endow blind band evaluation with cyclic selectivity.
- An improved envelope spectrum is built via in-band coherence integration.
- Experiments prove ARCCgram robustly locates fault bands under intense noise.

1. Introduction

As one of the indispensable load-bearing elements within rotating machinery, the rolling bearings are widely deployed in wind power generation, aerospace, and rail transit equipment. Prolonged exposure to high rotational speeds and heavy alternating contact stresses renders them inherently prone to localized surface damage [1–7]. Undetected defects can lead to unscheduled downtime or catastrophic mechanical failures. Developing reliable fault diagnosis techniques is therefore of considerable engineering importance for ensuring operational safety and curtailing through-life maintenance costs [8–11].

In envelope analysis, frequency band selection (FBS) serves as a critical preprocessing step for identifying the optimal demodulation band to extract fault modulated information from the broadband vibration spectrum as effectively as possible. By isolating the resonance band excited with fault-induced impulses, FBS suppresses background noise and interference, thereby enhancing diagnostic sensitivity. In a systematic study, Smith [12] categorized FBS techniques into blind and targeted methods. For the blind methods optimize bands on the basis of signal statistical properties without relying on require prior knowledge of the fault characteristic frequency (FCF). Conversely, for the targeted methods leverage known FCFs to construct dedicated indicators, achieving more precise band localization by focusing on specific fault-related cyclic

components.

For the blind methods, the Fast kurtogram [13] established a seminal framework for FBS, employing a 1/3-binary-tree filter bank to optimize sub-bands via temporal kurtosis. However, kurtosis captures non-Gaussian impulsivity regardless of its source, rendering it susceptible to selection bias under non-fault interference [14]. To enhance robustness, derivatives such as the adaptive kurtogram, Fast Entrogram, and Sparsogram were developed. Furthermore, the Infogram [15] integrates temporal impulsiveness with spectral periodicity, while the Autogram [16] evaluates squared envelope autocorrelation to suppress aperiodic impulses. Beyond filter bank structures, decomposition-based approaches like parameter-adaptive variational mode decomposition [17] and alternative criteria, such as conditional variance [18] and smoothness indices have further diversified the statistical perspectives of band evaluation. Nevertheless, these methods share a fundamental limitation: the lack of prior FCF information. Consequently, they often fail to distinguish fault signatures from fault irrelevant cyclostationary interference, leading to potential band-selection bias in complex environments.

In contrast, the targeted methods utilize prior FCF information to construct dedicated indicators, enabling precise band localization by focusing on fault related cyclostationary components [19]. Borghesani et al. [20] introduced the ratio of cyclic content (RCC), which evaluates the proportion of squared envelope spectrum (SES) energy contained in a frequency window centered on the target FCF, thereby imparting cyclic frequency selectivity to kurtosis. To enhance statistical stability, Liu et al. [21] developed a low variance RCC to address the high estimation variance of higher-order moments. Mo et al. [22] introduced the weighted cyclic harmonic to-noise ratio to capture multi-order harmonic information for complex fault patterns. Additionally, Borghesani et al. [23,24] presented the log cycligram based on the indicator of second-order cyclostationarity (ICS2), effectively decoupling cyclostationarity from non-Gaussianity. While superior in accuracy under complex interference, these methods fundamentally depend on a precisely pre-specified FCF. This reliance restricts their applicability when bearing geometry is unknown or fault types are unidentified. Recently, Cheng et al. [25] developed the IESCFFOgram for blind band selection using spectral coherence peaks. However, this method is vulnerable to energy leakage caused by speed jitter and relies on heuristic cyclic frequency selectivity rather than rigorous kurtosis theory. Thus, the convenience of blind operation and the rigor of targeted evaluation remain unintegrated.

In summary, aforementioned FBS methods still face two inherent drawbacks: (1) the blind methods without prior information and offer broad applicability, yet lack sufficient robustness when multiple cyclostationary interference sources coexist; (2) the targeted methods possess stronger interference rejection capability and band localization accuracy, yet their dependence on FCF prior knowledge restricts generalizability under practical operating conditions.

To overcome the aforementioned issues, this paper proposes an adaptive ratio of cyclic content gram (ARCCgram) method. In the ARCCgram method, the fast spectral coherence (SCoh) is first employed to extract the second-order cyclostationary (CS2) properties. Next, the multi-scale local-maximum detection is applied along the cyclic frequency axis to automatically capture candidate fault frequencies (CFFs), and the ARCC indicator is defined. The ARCC indicator maintains sensitivity to cyclostationary features while eliminating the dependence on theoretical FCFs. Then, by integrating ARCC into a 1/3-binary-tree framework, resulting ARCCgram effectively suppresses random impulses and discrete harmonics. This approach unifies the flexibility of blind methods with the interference rejection capability of targeted ones. Finally, the improved envelope spectrum (IES) is constructed through the integration of SCoh over the optimal band. The validation results show that ARCCgram performs better than state-of-the-art methods in fault feature extraction.

The main contributions of this work are summarized as follows:

(1) A novel ARCCgram framework is proposed by constructing an ARCC indicator via automatic fault frequency extraction from spectral coherence maps, achieving cyclic frequency selectivity without theoretical fault priors.

(2) The IES is constructed by restricting spectral coherence integration strictly to the identified optimal band, which can effectively suppresses out-of-band interference and robustly preserves fault harmonic structures.

(3) Comparative experiments demonstrate that the ARCCgram consistently outperforms state-of-the-art methods in accurate band localization and yields the highest adjusted diagnostic feature (ADF) values.

The paper is arranged as follows. Section 2 reviews the theoretical foundations of the RCC and the SCoh based enhanced envelope spectrum (EES). Section 3 introduces the proposed ARCCgram method and highlights how its SCoh based automated frequency identification mechanism removes the dependence on theoretical FCFs. Section 4 further examines the diagnostic robustness of the method under realistic operating conditions using multiple experimental bearing datasets. Section 5 concludes the paper.

2. Theoretical background

2.1. Ratio of cyclic content

Let $x(t)$ denote the collected vibration signal, with $\{x[n]\}_{n=1}^{L}$ being the finite-length discrete sampling sequence obtained from $x(t)$. Hereafter, continuous- and discrete-time signal representations are used interchangeably to best illustrate the mathematical derivation of the condition indicators. After bandpass filtering with center frequency f_c and bandwidth B, the filtered signal x_f[n] is obtained, and the squared envelope (SE) is defined in Eq. (1).

$$\mathrm{SE}[n] = |x_f[n] + j\mathrm{Hilbert}\{x_f[n]\}|^2 \tag{1}$$

where j stands for the imaginary unit, Hilbert$\{\cdot\}$ denotes the Hilbert transform, whose frequency response is $-j\,sgn(f)$. At nonzero frequencies, it preserves the amplitude and shifts the phase of each positive frequency component by -π/2. The transform is implemented using the FFT as $H\{x_f\}[n] = \mathrm{IDFT}\{-j\,sgn(k)X_f[k]\}$, $X_f[k] = \mathrm{DFT}\{x_f[n]\}$, where N is the length of the filtered signal $x_f[n]$. Thus, the expression in brackets in Eq. (1) is the analytic representation of $x_f[n]$, and its squared magnitude gives the squared envelope.

The SES is obtained from the squared magnitude of the discrete Fourier transform applied to the SE. The discrete spectral peaks of SES at the FCF and its harmonics are important indicators for diagnosing the presence and type of bearing faults.

$$\mathrm{SES}[k] = |DFT\{\mathrm{SE}|n|\}|^2 \tag{2}$$

Based on the analytical relationship between fourth-order statistics and SES, Borghesani et al [20] revealed the mathematical mechanism underlying the effectiveness of the Kurtogram method. For an analytic signal within the band-pass filtering band [l, h], kurtosis is defined as the ratio of the fourth-order moment to the squared second-order moment:

$$\kappa_{l,h} = \frac{m_4\{\tilde{x}_{l,h}[n]\}}{(m_2\{\tilde{x}_{l,h}[n]\})^2} \tag{3}$$

where $m_4\{\}$ and $m_2\{\}$ represent the fourth-order moment and the second-order moment, respectively. These moments are defined as $m_r\{\cdot\} = N^{-1}\sum_{n=1}^{N}|\cdot|^r$, where$\tilde{x}_{l,h}[n]$ is the analytic signal constructed according to Eq. (1) after filtering the signal within the frequency band [l, h].

For a zero-mean signal, the moments about the origin are equal to the central moments. By applying the Parseval theorem, the following identity can be proven.

$$\sum_{k=0}^{h-l} S\,\mathrm{ES}_{l,h}[k] = m_4\{\tilde{x}_{l,h}[n]\} \tag{4}$$

where the upper limit of summation equals the number of spectral lines within the frequency band [l, h], and $\mathrm{RMS}_{l,h} = \left(m_2\{\tilde{x}_{l,h}[n]\}\right)^{1/2}$ is the root mean square value of the analytic signal in that band.

$$\mathrm{SES}_{l,h}[0] = \mathrm{RMS}_{l,h}^4 \tag{5}$$

Eq. (4) indicates that all spectral line amplitudes in the SES add up to the fourth-order moment of the filtered analytic signal, whereas Eq. (5) shows that the SES value at zero cyclic frequency equals the fourth power of the root mean square (RMS) value of the signal. As can be known in Eqs. (3)-(5), a substantial increase in SES amplitudes at the FCF and its harmonics relative to the background noise directly elevates the kurtosis of the filtered band. However, due to the kurtosis indicator responds uniformly to all cyclic components within the SES, it inherently fails to differentiate genuine fault-induced periodic signatures from fault-irrelevant cyclic interference.

Limit the summation interval of the SES to the neighborhood [p, q] of the target cyclic frequency, and define the local kurtosis within this frequency band as follows:

$$\kappa_{l,h}^{p,q} = \frac{\sum_{k=p}^{q} S\mathrm{ES}_{l,h}[k]}{\mathrm{RMS}_{l,h}^4} \tag{6}$$

where the endpoints are defined as $p = [(f_{\mathrm{FCF}} - \Delta)/\Delta_\alpha]$, $q = [(f_{\mathrm{FCF}} + \Delta)/\Delta_\alpha]$, is the target fault characteristic frequency, Δ is the half width of the selected neighbourhood.

To endow the kurtosis indicator with cyclic-frequency selectivity, the RCC indicator was further proposed by Borghesani et al. [20]. The RCC is defined as the ratio of the

local kurtosis to the full-band kurtosis in Eq. (7).

$$\mathrm{RCC}_{l,h}^{p,q} = \frac{\kappa_{l,h}^{p,q}}{\kappa_{l,h}} = \frac{\sum_{k=p}^{q} \mathrm{SES}_{l,h}[k]}{\sum_{k=0}^{h-l} \mathrm{SES}_{l,h}[k]} \quad (7)$$

In engineering practice, to more accurately quantify the proportion of cyclic energy within the target FCF neighborhood relative to the non-DC cyclic energy, the DC component in the denominator can be excluded:

$$\mathrm{RCC}_{l,h}^{p,q} = \frac{\sum_{k=p}^{q} \mathrm{SES}_{l,h}[k]}{\sum_{k=1}^{h-l} \mathrm{SES}_{l,h}[k]} \quad (8)$$

When the integration interval $[p, q]$ is set around the theoretical FCF neighborhood, the RCC can effectively suppress the influence of cyclic components unrelated to bearing faults on the band optimization results. However, the calculation of the conventional RCC requires prior knowledge of the theoretical FCF to construct the cyclic frequency integration window, which is infeasible when bearing geometric parameters are unavailable or the fault type is unidentified.

2.2. Spectral coherence

In recent years, the second-order cyclostationary analysis framework based on SCoh has attracted considerable attention because it can simultaneously reveal the correlative structure across the carrier frequency domain and the modulation frequency domain [26,27].

To introduce the theoretical background of spectral coherence analysis, we first consider an ideal second order cyclostationary signal model. For a signal $x(t)$ satisfying this model, its autocorrelation function varies periodically with time, as expressed in Eq. (9):

$$R_x(t_n, \tau_m) = E\{x(t_n)x(t_n - \tau_m)^*\} = R_x(t_n + T, \tau_m) \quad (9)$$

where * denotes the complex conjugate, $E\{\bullet\}$ denotes the statistical expectation operator, T is the cyclic period. In actual bearings, timing jitter associated with rolling element positions within the cage clearance should be distinguished from random variations in cage speed. Under the relevant model assumptions, the former does not accumulate and can preserve CS2 properties, whereas the latter can produce PCS behaviour, with broadening of the fault spectral components increasing with harmonic order [28]. Eq. (9) is therefore used as a reference model rather than a strict assumption for all measured signals. For PCS components, "harmonics" refers to narrow spectral bands whose characteristic frequencies are approximately related by integer multiples within the analysed record [29].

The spectral correlation function is obtained by applying the double Fourier transform with respect to t and τ to the instantaneous autocorrelation function. The spectral correlation (SC) method is a second-order cyclic statistic that characterizes the statistical properties of CS2 signals by mapping time domain vibration signals onto a bifrequency plane spanned by the spectral frequency f and the cyclic frequency α, thereby revealing the modulation relationships among different frequency components. SCoh corresponds to the normalized form of the SC, and its magnitude is limited to the interval [0, 1]. It characterizes the correlation between the two spectral components located at frequencies f and $f + \alpha$.

$$\gamma_x(\alpha, f) = \frac{S_x(\alpha, f)}{\sqrt{S_x(0, f) \cdot S_x(0, f-\alpha)}} \quad (10)$$

where $S_x(\alpha, f)$ represents spectral correlation function, $S_x(0, f)$ indicate the classical power spectral density.

Integrating the SCoh along the spectral-frequency axis over the full frequency range yields the EES:

$$\mathrm{EES}(\alpha) = \frac{2}{F_s} \int_0^{F_s/2} |\gamma_x(\alpha, f)| df \quad (11)$$

where F_s denotes the sampling frequency.

If fault diagnostic information is uneven over the carrier frequency dimension, the full band integrated EES becomes vulnerable to strong background noise, which can mask the FCF features. Therefore, how to adaptively determine the carrier frequency integration interval that is rich in fault related information constitutes the key to improving the diagnostic performance of the envelope spectrum.

3. Proposed method

As discussed above, conventional targeted indicators such as the RCC are strictly dependent upon theoretical FCFs, whereas blind methods are frequently subject to band selection bias in the presence of strong interference. To address these inherent limitations, an ARCCgram based scheme for optimal demodulation band selection in rolling bearings is proposed. The flowchart of the proposed ARCCgram is given in Fig. 1. Then, the detailed instructions of the proposed ARCCgram are given in Subsection 3.2 to 3.4.

3.1. Overview of the proposed workflow

Step 1: *The Test rig and data collection.* The test rig acquires the vibration signal of the tested bearing at a sampling

frequency of F_s.

Step 2: *Adaptive extraction of candidate fault frequencies.* The Fast SCoh is utilized to find cyclic frequencies that repeatedly appear as local maxima in different spectral slices. The frequencies with the largest occurrence counts are retained as CFFs [30], and a small tolerance window is set around each one.

Step 3: *Optimal band selection based on the ARCC index.* The signal is decomposed into candidate bands by a 1/3-binary-tree filter bank. These bands define the search space for resonance band selection. For each candidate band, the SES is calculated and evaluated by ARCC. The band with the maximum ARCC is selected as the optimal demodulation band.

Step 4: *Construction of the improved envelope spectrum.* The IES is constructed by integrating SCoh over the spectral-frequency axis within the optimal band. The fault type is then determined from the prominent FCF peak and its harmonics in the IES.

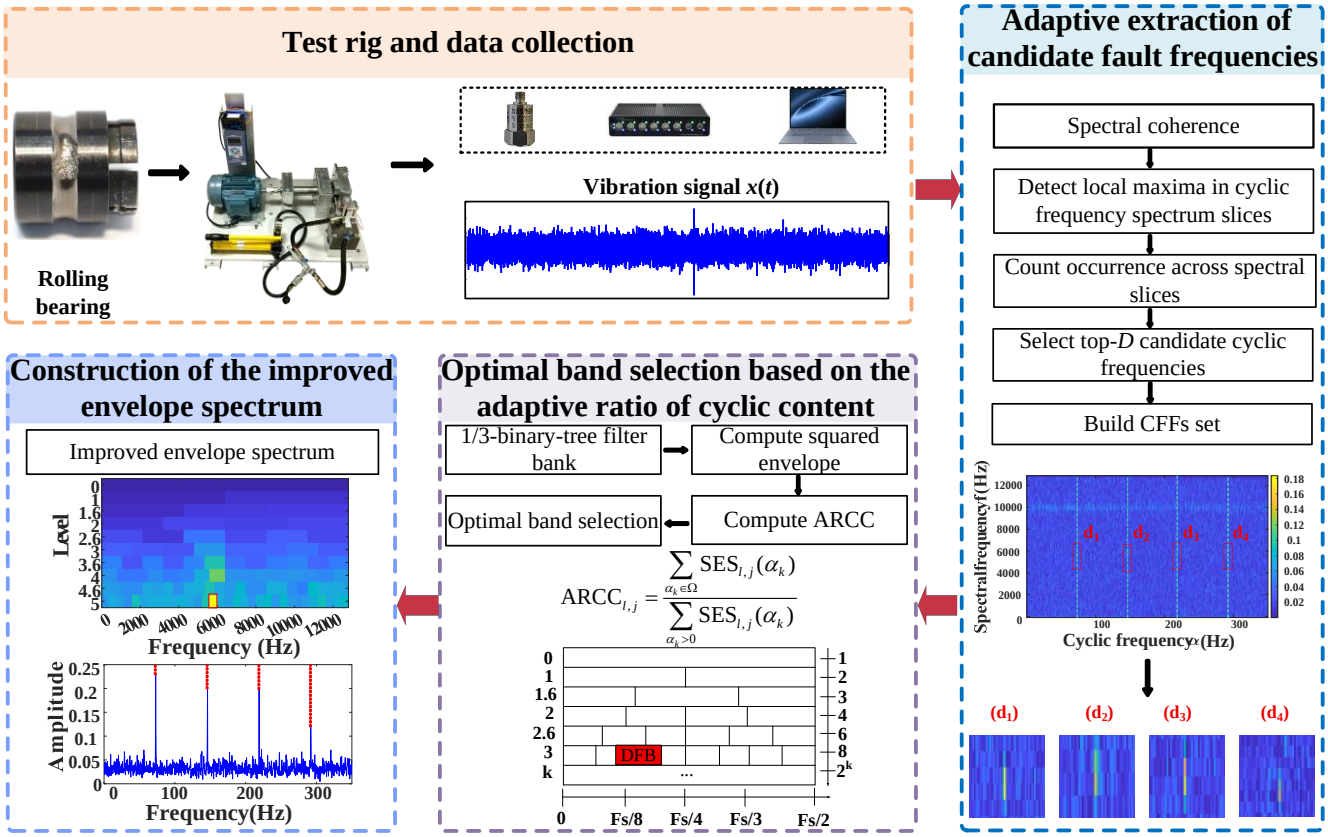


Figure 1. The flowchart of the proposed ARCCgram.

3.2. Adaptive extraction of candidate fault frequencies

For a finite record with relatively concentrated fault components, local maxima may recur at similar cyclic frequencies across multiple spectral frequency slices. Their occurrence counts are therefore used to extract candidate frequencies. Appreciable PCS broadening may distribute these maxima across neighbouring cyclic frequency bins and affect the candidate ranking. This procedure therefore does not establish whether a signal is strictly CS2. The number of non-zero elements in the n-th row of the matrix ξ reflects how frequently the cyclic frequency α_n is identified as a local maximum across all CFSSs. A frequency count vector is defined $\eta = [\eta(1), \eta(2), \ldots, \eta(N_\alpha)]^T$, whose n-th element is given by:

$$\eta(n) = \sum_{g=1}^{N_f} \xi(n, g), n = 1,2, \ldots, N \qquad (12)$$

The larger the value of $\eta(n)$, the more likely the cyclic frequency is the periodic modulation frequency actually present in the signal.

Sorting η in descending order yields to the ranked sequence $\tilde{\eta} = [\tilde{\eta}(1), \tilde{\eta}(2), \ldots, \tilde{\eta}(N_\alpha)]$, from which the top D cyclic frequencies with the highest counts are selected as the CFFs set:

$$\hat{\alpha}(d) = \{\alpha_n \mid \eta(n) = \tilde{\eta}(d),\ n = 1,2, \ldots, N_\alpha\}, d = 1,2, \ldots, D \qquad (13)$$

The parameter D is determined in proportion to the maximum cyclic frequency α_{max}:

$$D = p_1 \cdot \alpha_{max} \tag{14}$$

where p_1 is a proportional coefficient with a recommended range of 1%-10%. This parameterized design ensures that the number of CFFs scales with the analyzed frequency range and remains independent of the cyclic-frequency resolution.

A local tolerance window is introduced to collect spectral values near each candidate frequency. Its half-width is set to $2\Delta_\alpha$, whereΔ_α is the cyclic frequency grid spacing. This width is determined by the grid rather than an estimate of physical spectral broadening and may not fully cover appreciably broadened components at higher orders.

$$\delta_\alpha = 2\Delta_\alpha \tag{15}$$

The tolerance window corresponding to the d-th CFF is then given by:

$$W_d = [\hat{\alpha}(d) - \delta_\alpha, \hat{\alpha}(d) + \delta_\alpha] \tag{16}$$

3.3. Optimal band selection based on the adaptive ratio of cyclic content

The ARCCgram adopts the 1/3-binary-tree filter bank [31] to generate the search space for resonance band localization. By inserting intermediate trisection levels between adjacent binary levels, this structure provides a favorable trade-off between frequency resolution and computational efficiency. Within this multiresolution framework, each candidate sub-band $B_{l,\ j}$ is characterized by its decomposition level l and band index j, and bandpass filtering is realized in the frequency domain through FFT-based masking, yielding the narrowband signal $x_{l,j}[n]$ for each sub-band.

For the narrowband signal, the Hilbert transform is used to form the analytic signal as $z_{l,j}[n] = x_{l,j}[n] + j \cdot H\{x_{l,j}[n]\}$, from which the squared envelope is obtained as $s_{l,j}[n] = e_{l,j}^2[n]$. The SES, which serves as the analytical foundation for evaluating the cyclostationary content of each sub-band, is defined as the squared modulus of the discrete Fourier transform of $s_{l,j}[n]$:

$$\mathrm{SES}_{l,j}(\alpha_k) = \left|\sum_{n=0}^{N-1} s_{l,j}\,[n] \cdot exp\left(-j2\pi \frac{\alpha_k}{F_s} n\right)\right|^2 \tag{17}$$

where $\alpha_k = k\frac{F_s}{N}(k = 0,1,\ldots,\frac{N}{2})$, denotes the discrete cyclic frequency. Here, N denotes the length of the subband signal after downsampling. Consequently, the cyclic frequency resolution Δ_α varies with the decomposition level l.

By combining the automatic CFF extraction mechanism established in Subsection 3.2 with the sub-band SES computation, the ARCC indicator is defined as the ratio of the SES energy concentrated within the union of CFF tolerance windows Ω to the total non-DC SES energy over the full cyclic-frequency range:

$$\mathrm{ARCC}_{l,j} = \frac{\sum_{\alpha_k \in \Omega} \mathrm{SES}_{l,j}(\alpha_k)}{\sum_{\alpha_k > 0} \mathrm{SES}_{l,j}(\alpha_k)} \tag{18}$$

The physical interpretation of Eq. (18) is twofold. On the one hand, it quantifies the proportion of SES energy within sub-band $B_{l,j}$ that is concentrated near the data-driven candidate fault frequencies, thereby characterizing the density of fault-related cyclic components within the band. It inherits the cyclic-frequency selectivity of the conventional RCC while dispensing with the requirement for theoretical FCFs, which achieves a blind treatment with respect to bearing geometric parameters and substantially broadens the engineering applicability of the method.

By traversing all decomposition levels and band positions within the 1/3-binary-tree, the ARCC values at all nodes are assembled into a two-dimensional ARCCgram map. The optimal demodulation band $B_{l^*j^*}$ is subsequently identified as the sub-band maximizing the ARCC:

$$(l^*, j^*) = argmax_{l \in \mathcal{L},\ 1 \le j \le n_B(l)} \mathrm{ARCC}_{l,j} \tag{19}$$

where $\mathcal{L}$ denotes the set of admissible decomposition levels and $n_B(l)$ is the number of sub-bands at level l. Eq. (19) connects band evaluation to band selection in ARCCgram. Eq. (18) assigns an ARCC value to each node of the 1/3-binary tree, and these values form the two-dimensional ARCCgram map. Eq. (19) then selects a subband (l^*, j^*). with the largest ARCC value. Since the feasible domain consists of a finite set of discrete nodes, exhaustive evaluation yields a global maximum of the ARCC objective within the prescribed grid. The selected pair (l^*, j^*) determines the frequency band $[f_1, f_2] = [(j^* - 1)B_{l^*},\ j^*B_{l^*}]$, whose boundaries define the limits of spectral coherence integration in Eqs. (20) and (21). In each ARCCgram plot, the node outlined in red represents the selected solution, while B_w and f_c in the plot title denote its bandwidth and centre frequency, respectively.

3.4. Construction of the improved envelope spectrum

Once the optimal demodulation band has been determined via the ARCCgram, the spectral coherence is integrated within that band to construct the final diagnostic spectrum. As discussed in Subsection 2.2, the EES obtained through full-band integration

is susceptible to out-of-band noise contamination, which limits its diagnostic performance. To solve this shortcoming, the integration interval of the SCoh is restricted to the spectral-frequency range corresponding to the optimal band, and the IES is defined as:

$$\mathrm{IES}(\alpha) = \frac{1}{f_2 - f_1} \int_{f_1}^{f_2} |\gamma_x(\alpha, f)| df \tag{20}$$

Compared with the EES, the IES integrates the spectral coherence along the spectral-frequency axis within the optimal band, thereby effectively suppressing interference from out-of-band noise components. For discrete implementation, Eq. (20) is reformulated as:

$$\mathrm{IES}(\alpha_n) = \frac{1}{N_f^*} \sum_{g: f_g \in \mathcal{B}^*} \left|\hat{\gamma}_x(\alpha_n, f_g)\right|, n \geq 2 \ (\alpha_n \neq 0) \tag{21}$$

where N_f^* denotes the number of discrete spectral frequency points within the optimal band. Peaks or narrow spectral families associated with the fault, together with their sideband structures in the IES, provide evidence for bearing fault identification.

Algorithm 1 ARCCgram

Input:
Vibration signal $x[n]$; sampling frequency F_s; maximum cyclic frequency $\alpha_{\max}$; candidate coefficient p_1; admissible decomposition levels $\mathcal{L}$.

Output: ARCCgram map A; optimal demodulation band $B^\star$; improved envelope spectrum IES.

Candidate frequency extraction

Compute the fast spectral coherence $\hat{\gamma}_x(\alpha_n, f_g)$ of $x[n]$

Construct $\xi(n, g)$ from local maxima along the cyclic frequency axis of each spectral slice

$$\eta(n) \leftarrow \sum_{g=1}^{N_f} \xi(n, g) \qquad \text{Eq.(12)}$$

$$D \leftarrow p_1 \alpha_{\max} \qquad \text{Eq.(14)}$$

Sort $\eta(n)$ in descending order and obtain $\hat{\alpha}(d)$, $d = 1, \ldots, D$, using Eq. (13)

$$\delta_\alpha \leftarrow 2\Delta_\alpha \qquad \text{Eq.(15)}$$

$$W_d \leftarrow [\hat{\alpha}(d) - \delta_\alpha, \hat{\alpha}(d) + \delta_\alpha], \ d = 1, \ldots, D$$

$$\Omega \leftarrow \bigcup_{d=1}^{D} W_d$$

Band evaluation and selection

Construct the candidate bands $B_{\ell,j}$ using the 1/3-binary tree

for each $\ell \in \mathcal{L}$ **do**

  for $j = 1, \ldots, n_B(\ell)$ **do**

    Obtain $x_{\ell,j}[n]$ by FFT masking within $B_{\ell,j}$

    Form the analytic signal $z_{\ell,j}[n]$ and its squared envelope $s_{\ell,j}[n]$

    Compute $\mathrm{SES}_{\ell,j}(\alpha_k)$ using Eq. (17)

$$\mathrm{ARCC}_{\ell,j} \leftarrow \frac{\sum_{\alpha_k \in \Omega} \mathrm{SES}_{\ell,j}(\alpha_k)}{\sum_{\alpha_k > 0} \mathrm{SES}_{\ell,j}(\alpha_k)} \qquad \text{Eq.(18)}$$

$$A(\ell, j) \leftarrow \mathrm{ARCC}_{\ell,j}$$

  end for

end for

$$(\ell^\star, j^\star) \leftarrow \underset{\ell \in \mathcal{L},\, 1 \leq j \leq n_B(\ell)}{\operatorname{argmax}} \mathrm{ARCC}_{\ell,j} \qquad \text{Eq.(19)}$$

$$B^\star \leftarrow B_{\ell^\star, j^\star}$$

IES construction

$$N_f^\star \leftarrow |\{g : f_g \in B^\star\}|$$

$$\mathrm{IES}(\alpha_n) \leftarrow \left(N_f^\star\right)^{-1} \sum_{g: f_g \in B^\star} |\hat{\gamma}_x(\alpha_n, f_g)|, \ \alpha_n \neq 0 \qquad \text{Eq.(20)}$$

return $A, B^\star$, IES

4. Simulation study

To validate the band localization and fault feature extraction capabilities of ARCCgram under background noise, discrete harmonic interference and random external impulses, this section constructs a bearing fault simulation model consistent with engineering dynamics. The simulated signal is generated using a classical four-component model comprising fault impulses, discrete harmonics, random impulses, and additive noise. This model ensures the coexistence of CS2 fault components and random impulse interference that lacks cyclostationarity, thereby providing a rigorous testbed for

evaluating the robustness of band selection algorithms against interference.

4.1. Simulation model and parameter settings

Based on the dynamic response mechanism by which a localized bearing defect excites structural resonances, a composite signal is constructed as: [25]

$$x(t) = b(t) + h(t) + r(t) + n(t) \quad (22)$$

where $b(t)$, $h(t)$, $r(t)$, and $n(t)$ denote the periodic fault impulse component, the shaft-related discrete harmonic interference, the aperiodic random external impulse, and the additive white Gaussian background noise, respectively, with the signal-to-noise (SNR) of the latter equal to -18 dB.

When the localized defect repeatedly excites structural resonances at the FCF f_m, the fault impulse component can be described by a superposition of damped oscillations:

$$b(t) = \sum_{i=1}^{M_1} A_i \cdot e^{-2\pi\xi_1 f_{n,1}\left(t-\frac{i}{f_m}-\delta_i\right)} sin(2\pi\sqrt{1-\xi_1^2} f_{n,1}\left(t-\frac{i}{f_m}-\delta_i\right) \quad (23)$$

where $f_{n,1}$ and ξ_1 represent the resonance frequencies and damping ratio excited by the fault impulses, respectively; M_1 means the total number of impulses within the sampling duration (approximately $M_1 \approx f_m T$); δ_i represents minor fluctuations in the arrival time caused by rolling element slippage, introduced to capture realistic speed perturbations and slippage effects. For outer-race faults, the impulse amplitude is typically set to $A_i = 1$.

The discrete harmonic component is employed to simulate deterministic narrowband interference arising from shaft misalignment, structural looseness, or rotational-frequency-related excitations, and is expressed as:

$$h(t) = \sum_{j=1}^{M_2} B_j \, sin(2\pi f_j t + \varphi_j) \quad (24)$$

where M_2 denotes how many harmonic terms are included, and f_j, B_j, and φ_j correspond respectively to the frequency, amplitude, and initial phase of the j-th harmonic.

The random external impulse component is used to simulate strong impulsive interference that lacks cyclostationary properties, such as environmental impacts, electromagnetic disturbances, or occasional collisions:

$$r(t) = \sum_{k=1}^{M_3} c_k e^{-2\pi\xi_3 f_{n,3}(t-\tau_k)} \, sin(2\pi f_{n,3}\sqrt{1-\xi_3^2}(t-\tau_k)) u(t-\tau_k) \quad (25)$$

where M_3 denotes how many random impulses are included; C_k and τ_k correspond respectively to the amplitude and occurrence time of the k-th random impulse; $f_{n,3}$ and ξ_3 denote the resonance frequency and damping ratio associated with the random impulses. In this study, the simulated signals use a sampling duration of 3 s and a sampling frequency of 25.6 kHz. All aforementioned parameter values are given in Tables 1 and 2.

Table 1. Parameter settings for the simulated outer-race bearing fault impulse components.

Parameter	M_1	f_m(Hz)	f_r(Hz)	$f_{n,1}$(Hz)	ξ_1
Value	219	73	10	5800	0.02

Table 2. Simulation parameters of the discrete harmonic component.

Parameter	M2	B1	B2	f1(Hz)	f2(Hz)	φ_1	φ_2
Value	2	0.05	0.05	10	20	$\pi/6$	$-\pi/3$

4.2. Outer-race fault with single resonance

An outer-race fault rolling bearing is used as the example, and Fig. 2 presents the simulated signal with a single resonance condition, and the value of SNR is set as -18 dB. Fig. 2(a) shows a one-second segment of the composite signal obtained by superimposing all components, and Fig. 2(b) displays the corresponding frequency spectrum. A distinct resonance band is visible near 5,800 Hz in Fig. 2(b).

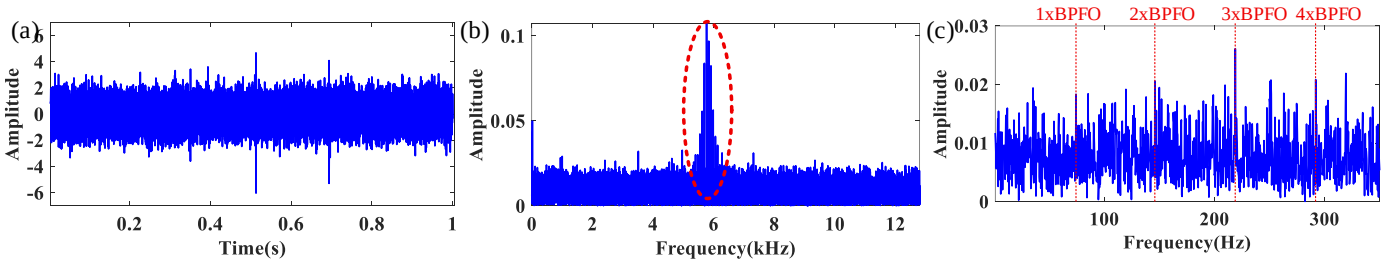


Figure 2. (a) the noisy signal, (b) the corresponding frequency spectrum, (c) The envelope spectrum of the original signal.

Fig. 3 compares the four methods on this simulated signal. The maximum cyclic frequency is set to 350 Hz, covering the first four harmonics of the simulated fault repetition frequency f_m = 73 Hz. As seen in Figs. 3(a) and 3(b), the Fast kurtogram picks a band at 9,866.7 Hz that overlaps with the random-impulse resonance near 10,000 Hz rather than the fault impulse

resonance, so no FCF peak emerges in its SES. The Autogram in Figs. 3(c) and 3(d) is likewise drawn to the random-impulse band; only the fundamental is visible in its SES, while the second, third and fourth harmonics remain buried. From Figs. 3(e) and 3(f), the CFFsgram correctly localises the optimal demodulation band at 5,867 Hz, yet its weighted SES recovers only the fundamental, second and fourth harmonics, with the second reaching the largest peak and the third hidden by noise. By contrast, the ARCCgram in Figs. 3(g) and 3(h) locks the optimal band at 5,800 Hz, matching the fault-impulse resonance exactly; its IES resolves the first four FCF harmonics The corresponding IES in Fig. 3(h) resolves the first four harmonics of the simulated fault repetition frequency.

The above simulation results demonstrate that under conditions of strong noise combined with random impulse interference, the ARCCgram can adaptively lock onto the resonance band richest in fault information. This capability stems from its data-driven candidate fault frequency extraction and targeted band evaluation mechanism, which together yield diagnostic accuracy and interference rejection capability superior to those of the three comparison methods.

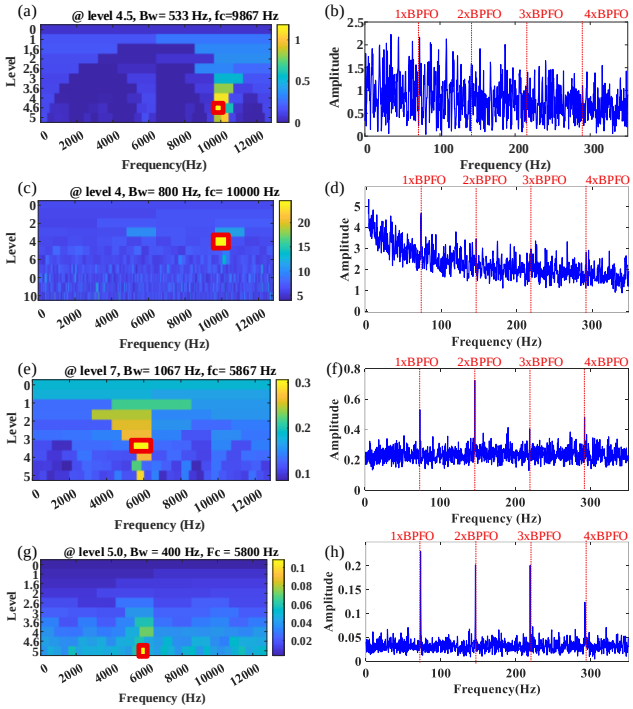


Figure 3. The results of rolling bearing simulated signal with outer race fault. (a) Fast kurtogram, (b) the SES of Fast kurtogram, (c) Autogram, (d) the SES of Autogram, (e) CFFsgram, (f) the SES of CFFsgram, (g) ARCCgram, (h) the IES of ARCCgram.

5. Experimental validation

5.1. BJTU-RAO dataset validation

As shown in Fig. 4(a), a fault simulation test rig built upon a 1:2 scaled metro train bogie transmission system was used to collect the experimental data. The tested bearing, mounted in the left axle box, is the double-row tapered roller bearing HRB 352213. The sampling frequency is F_s = 64 kHz. The outer-race fault specimen from this axle box bearing, shown in Fig. 4(b), was selected for assessing the diagnostic capability of the ARCCgram. The theoretical rotational frequency and the ball pass frequency of the outer race are f_r = 60 Hz and f_{BPFO} = 72.4 Hz, respectively.

Fig. 5 previews the raw signal. The time-domain waveform in Fig. 5(a) oscillates between -2.5 and 2.5 m/s² with occasional non-Gaussian spikes, yet the periodic fault impulses are buried under wheel-rail excitation and broadband noise. The FFT spectrum in Fig. 5(b) concentrates its energy in the low frequency range and a few mid-frequency resonance zones, offering no fault-related peak. In the Hilbert demodulated envelope spectrum of Fig. 5(c), no prominent line appears at the expected f_{BPFO} = 72.4 Hz, and the amplitudes around the second and third harmonics are either negligible or lost in noise. Direct envelope demodulation is therefore inadequate for revealing the outer-race fault signature under such operating conditions.

The comparative results of the four methods on this dataset are summarized in Fig. 6, where Figs. 6(a) and 6(b) present the Fast kurtogram and its SES. The Fast kurtogram selects a band centred at 26,000 Hz. The resulting SES exhibits peaks at the fundamental fault frequency and the second harmonic, yet higher order harmonics are absent. As can be seen in Figs. 6(c) and 6(d) that the fundamental and the second harmonic can be recognised, but the third harmonic is not detectable. Figs. 6(e) and 6(f) display the CFFsgram and its weighted SES. The CFFsgram identifies a band centred at 3,333 Hz as optimal. The fundamental fault frequency together with the second and third harmonics are visible in the weighted SES. Nevertheless, a conspicuous spurious peak appears between the second and third harmonics, which may mislead fault type identification. Figs. 6(g) and 6(h) present the ARCCgram and its IES. The ARCCgram selects 13,500 Hz as the optimal band centre. In the corresponding IES in Fig. 6(h), components associated with the

first four harmonics of f_{BPFO}, namely the fundamental and the second, third, and fourth harmonics, are clearly identifiable. No spurious peak of comparable magnitude is observed, yielding a clean diagnostic spectrum free from ambiguity.

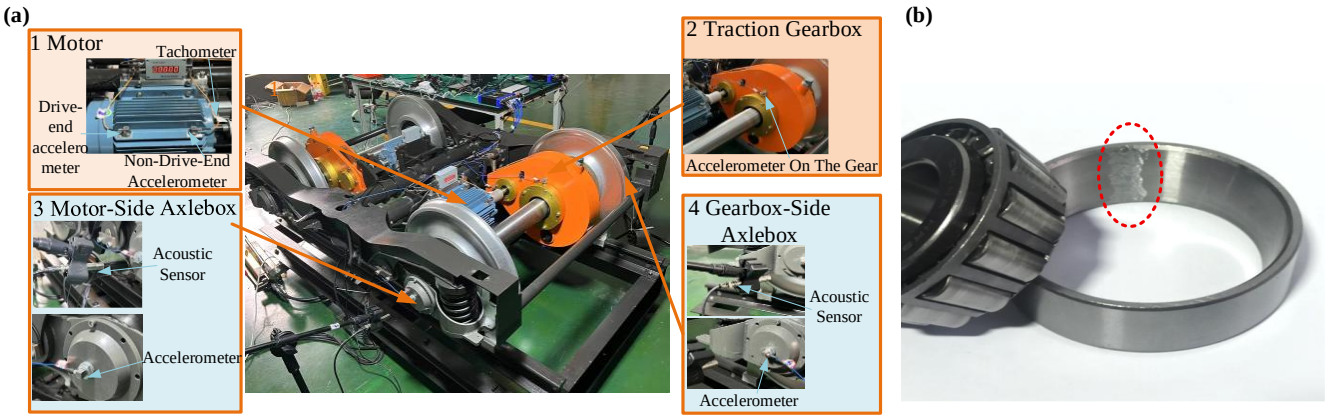


Figure 4. Experimental setup: (a) BJTU-RAO Bogie Dataset experiment test rig, (b) Bearing outer race fault.

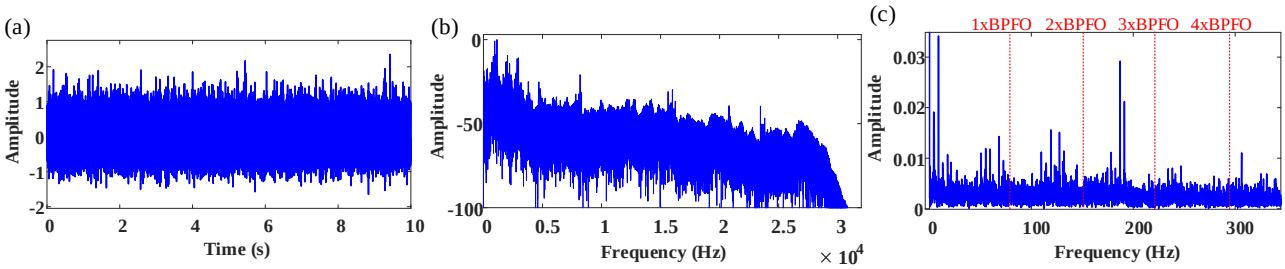


Figure 5. Time and frequency domain analysis of the raw outer-race fault signal from the BJTU-RAO dataset. (a) The time domain of the original signal, (b) Single-sided amplitude spectrum of the raw signal, expressed in dB relative to its largest non-DC amplitude, (c) the corresponding envelope spectrum.

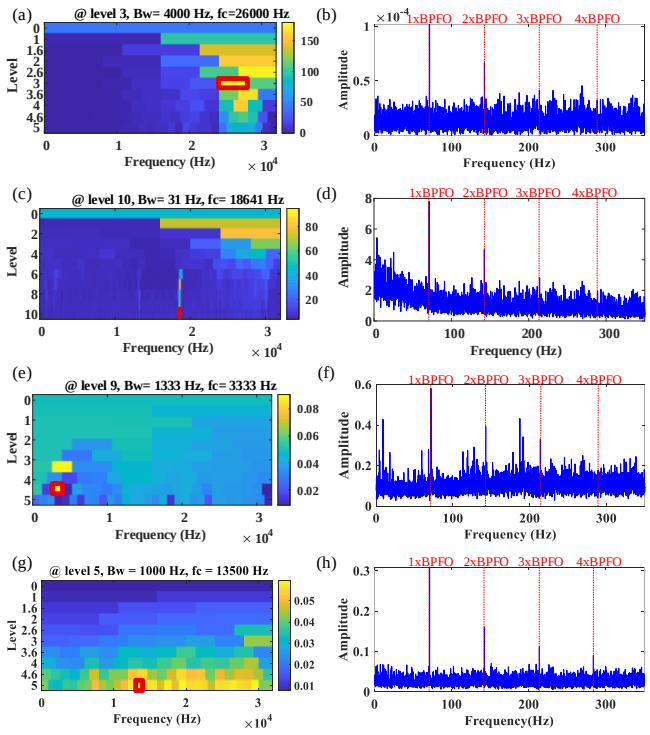


Figure 6. Bearing outer ring fault signal result. (a) Fast kurtogram. (b) the SES of Fast kurtogram, (c) Autogram, (d) the SES of Autogram, (e) CFFsgram, (f) the SES of CFFsgram, (g) ARCCgram, (h) the IES of ARCCgram.

These results indicate that, on the BJTU-RAO outer-race fault data, the ARCCgram provides the most reliable band selection among the four methods compared, producing an IES with the clearest harmonic structure and the least spectral

contamination.

5.2. XJTU-SY dataset validation

For inner-race fault analysis, this section uses the XJTU-SY accelerated life test dataset to further evaluate the proposed method. This dataset was released by the research group of Professor Lei Yaguo at Xi'an Jiaotong University. Different from the BJTU-RAO dataset, which relies on artificially seeded defects, the XJTU-SY dataset as shown in Fig. 7(a) captures the entire degradation process of bearings from their initial healthy state to eventual failure, thus better reflecting real industrial service conditions. Vibration signals were acquired at a sampling rate of F_s = 25.6 kHz . Bearing 2-1 under Operating Condition 2 is selected for validation, illustrated in Fig. 7(b). The rotational speed is 2,250 r/min and the radial load is 11 kN. Prolonged operation under this heavy load ultimately led to severe fatigue spalling on the inner race. The theoretical shaft rotational frequency and the inner-race FCF are f_r = 37.5 Hz and f_{BPFI} = 184.4 Hz, respectively.

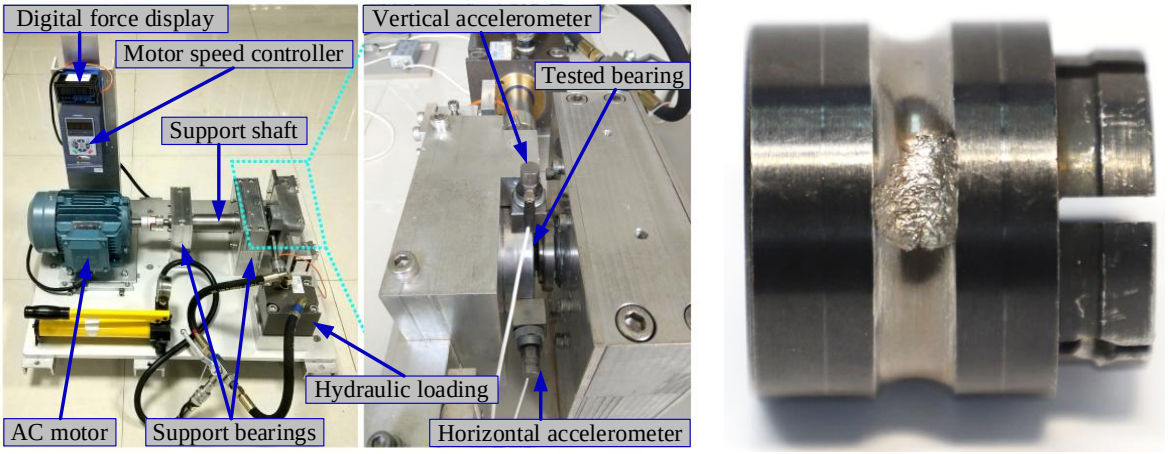


Figure 7. Experimental setup. (a) XJTU-SY rolling bearing accelerated life test rig, (b) Bearing inner race fault.

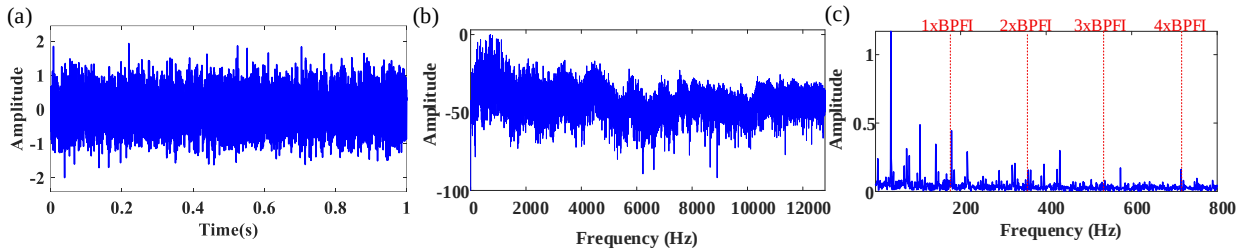


Figure 8. Time and frequency domain analysis of the raw inner-race fault signal from the XJTU-SY dataset: (a) The time domain of the original signal, (b) Single-sided amplitude spectrum of the raw signal, expressed in dB relative to its largest non-DC amplitude, (c) the corresponding envelope spectrum.

Fig. 8 shows the time domain and frequency domain characteristics of the raw vibration signal, with Fig. 8(a) showing the time domain waveform during the failure stage of Bearing 2-1. The frequency spectrum in Fig. 8(b) reveals a broadband and irregular energy distribution that offers no identifiable fault signature. Fig. 8(c) shows the envelope spectrum obtained by direct Hilbert demodulation. Although several peaks emerge in the low-frequency region, the spectral components near f_{BPFI} = 184.4 Hz remain weak and lack a recognisable harmonic series. This confirms that the rotational frequency modulation pattern characteristic of inner-race faults cannot be recovered by straightforward envelope analysis of the raw signal.

The comparative results of the four methods on this inner-race fault case are illustrated in Fig. 9, where Figs. 9(a) and 9(b) show the Fast kurtogram and its SES. The Fast kurtogram identifies a band centred at 11,200 Hz. The corresponding SES resolves only the fundamental and the second harmonic of f_{BPFI}. Figs. 9(c) and 9(d) present the Autogram and its SES. The fundamental and second harmonic are recognisable, yet the third harmonic remains indistinguishable from the noise floor. Figs. 9(e) and 9(f) give the CFFsgram and its weighted SES.

The CFFsgram places the optimal band at a centre frequency of 400 Hz. In the resulting weighted SES, none of the first four harmonics of f_{BPFI} can be reliably identified. Components at the shaft rotational frequency and its harmonics may arise from amplitude modulation of the inner race fault response. They should be interpreted together with the fault spectral families and sidebands spaced at the shaft frequency, rather than classified as interference unrelated to the fault solely because of their dominant amplitudes [3].Figs. 9(g) and 9(h) display the ARCCgram and its IES. The ARCCgram places the optimal band at a centre frequency of 1,200 Hz. The spectral families associated with the inner race fault and their neighbouring sidebands are clearly visible in Fig. 9(h). The sidebands spaced at the shaft rotational frequency are consistent with the modulation mechanism of an inner race fault and support fault identification in this case.

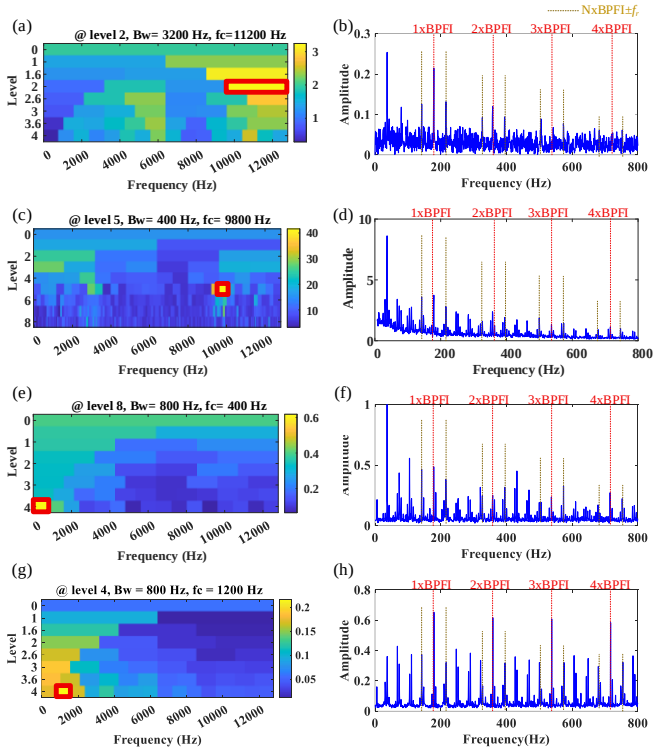


Figure 9. Bearing inner ring fault signal result. (a) Fast kurtogram, (b) the SES of Fast kurtogram, (c) Autogram, (d) the SES of Autogram, (e) CFFsgram, (f) the SES of CFFsgram, (g) ARCCgram, (h) the IES of ARCCgram.

5.3. Validation using a rolling-element fault test-bench dataset

The vibration signals analysed in this section were collected during a test-bench experiment conducted at a factory site, as shown in Fig. 10(a). A scratch measuring 0.1 mm in width and 0.43 mm in depth was introduced onto the rolling element surface by electrical discharge machining to replicate a localised defect, illustrated in Fig. 10(b). The motor operated at 1,169 r/min, and signals were sampled at 5,120 Hz. The kinematic BSF reference used in this study is 133 Hz. Slip may cause the observed characteristic frequency to differ from this value [3].

A preliminary time and frequency do main examination of the raw vibration signal is presented in Fig. 11, where Fig 11(a) shows the time domain waveform, whose amplitude spans roughly -5 to 5. The frequency spectrum in Fig. 11(b) is dominated by broadband energy spread across the entire analysed range, with no distinguishable spectral feature attributable to the rolling element defect. Groups of spectral peaks are visible in Fig. 11(c). Their association with the fault should be assessed by examining the centres of spectral families across several orders together with their sideband spacings. Frequency shifts caused by slip, as well as sideband asymmetry and weakening of the central components that may result from combined AM and PM, mean that local maxima need not coincide with the theoretical BSF or its integer multiples. The absence of dominant peaks at these theoretical frequencies is therefore insufficient to conclude that direct envelope analysis has failed to extract fault information.

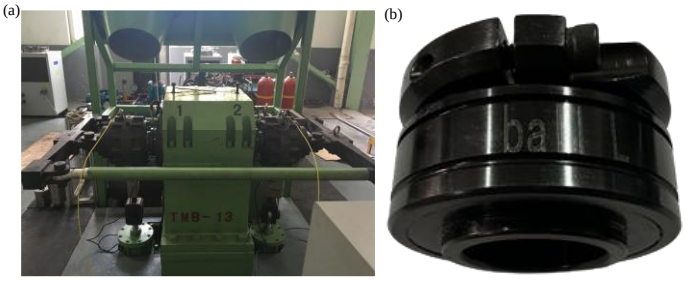


Figure 10. Experimental setup: (a) Fault test bench;(b) bearing rolling element fault.

The diagnostic results of the four methods are compared in Fig. 12. As shown in Figs. 12(a) and 12(b) that the Fast kurtogram and its SES with a selected band centred at 1,600 Hz and a bandwidth of 640 Hz. Groups of spectral peaks are visible near several nominal BSF orders, although their prominence varies against the surrounding background. Figs. 12(c) and 12(d) show the Autogram and its SES. The selected band is centred at 1,120 Hz with a bandwidth of 320 Hz. The spectral group near the first nominal BSF order is prominent, while the groups at higher orders are weaker. Figs. 12(e) and 12(f) show the

CFFsgram and its weighted SES, obtained from a band centred at 1,600 Hz with a bandwidth of 640 Hz. Components are also visible near the nominal BSF orders, with varying relative amplitudes of the central peaks and neighbouring sidebands. These spectra should be interpreted from the relationships among the spectral families and their sidebands, allowing for frequency shifts and modulation effects. Neither a weak component at a theoretical reference frequency nor a dominant low frequency peak alone establishes the absence of fault information or inadequate interference suppression. Figs. 12(g) and 12(h) show the ARCCgram and its IES. ARCCgram selects a band centred at 1,600 Hz with a bandwidth of 640 Hz. The IES presents relatively clear spectral families and neighbouring sidebands near the first four nominal BSF orders, supporting identification of the rolling element fault in this record. This interpretation does not require the largest peaks to coincide with the theoretical reference lines or their amplitudes to decrease monotonically with order. Since the Fast kurtogram, CFFsgram and ARCCgram select the same band, the differences in their final spectra also reflect their spectrum construction procedures and cannot be attributed to band selection alone.

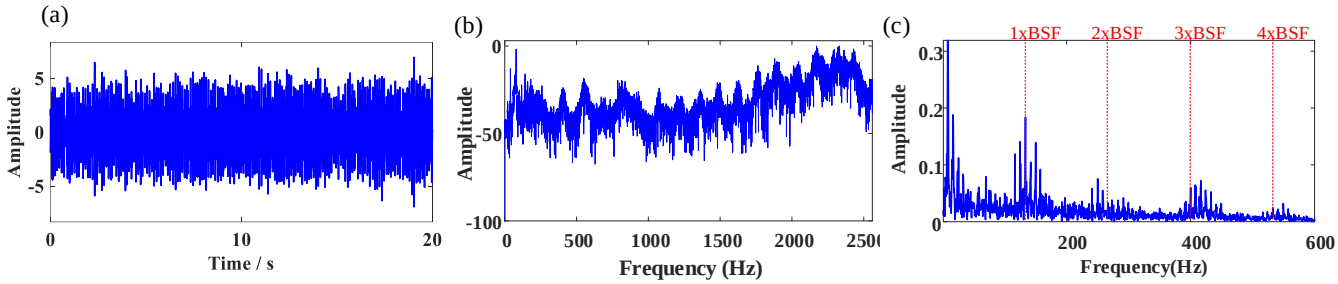


Figure 11. Time and frequency domain analysis of the raw rolling element fault signal collected from the test bench: (a) The time domain of the original signal, (b) Single-sided amplitude spectrum of the raw signal, expressed in dB relative to its largest non-DC amplitude, (c) the corresponding envelope spectrum.

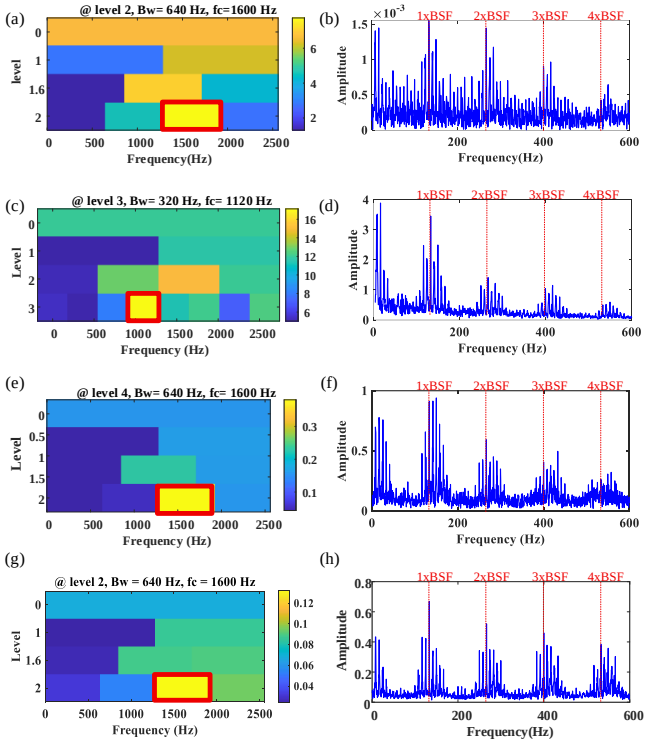


Figure 12. Comparison of the four methods for the rolling element fault record: (a) Fast kurtogram; (b) its SES; (c) Autogram; (d) its SES; (e) CFFsgram; (f) its weighted SES; (g) ARCCgram; and (h) its IES. The vertical reference lines denote the nominal BSF orders at 133, 266, 399 and 532 Hz. These kinematic references do not represent independently measured centres of the observed spectral families.

The results for this rolling-element fault case show that ARCCgram extracts identifiable fault-related spectral families

under the investigated test-bench conditions. Its performance in bearings operating in machines under actual service conditions requires further validation.

5.4. Performance evaluation

Through the preceding experimental validations on three datasets, the ARCCgram, Fast kurtogram, Autogram, and CFFsgram were compared regarding band localization accuracy and diagnostic spectral morphology. Typical observations include the tendency of conventional kurtosis- and autocorrelation-based methods to suffer from band-selection bias under random impulse and strong harmonic interference, which subsequently causes the FCF and its harmonics in the SES to be submerged in noise. In contrast, the ARCCgram leverages the cyclostationary information provided by the fast spectral coherence together with the data-driven CFF extraction mechanism to achieve adaptive locking onto the resonance band that is richest in fault-related cyclic components, and constructs the IES through spectral coherence integration within the optimal band, thereby yielding a clearer and more stable harmonic structure. To further quantify the comparative results, this paper adopts the ADF [25] indicator, which measures the prominence of the FCF and its harmonics relative to the local noise floor in the diagnostic spectrum. This indicator estimates the noise level within a narrow band around each harmonic and subtracts the local minimum, thereby mitigating the influence of spectral amplitude scaling on the evaluation outcome. The ADF is defined as follows:

$$ADF(f_m) = \frac{1}{H}\sum_{h=1}^{H} \frac{A(hf_m) - A_{min}}{\frac{1}{2f_b}\sum_{k=(hf_m-f_b)/\Delta f}^{(hf_m+f_b)/\Delta f} A(k\Delta f) - A_{min}} \tag{26}$$

where $A(f)$ denotes the value of the diagnostic spectrum at frequency f, and Δf denotes its discrete frequency-grid spacing, A_{min} is the minimum spectral amplitude within the narrow band $[hf_m - f_b, hf_m + f_b]$, f_b is the noise estimation bandwidth ($f_b = f_r/3$), and H denotes the number of harmonic orders included in the ADF calculation. Here, $H = 3$, so the calculation includes the fundamental and the second and third harmonics. The ADF in Eq. (26) evaluates spectral values at the harmonic reference frequencies. Frequency shifts or spectral broadening may reduce its representativeness of the associated spectral families. It is therefore used here as a supplementary measure for the analysed records; evaluation of broadened components would require aggregation over appropriate cyclic-frequency intervals and a corresponding treatment of the local spectral background. Fig. 13 presents the ADF comparison results across all three experiments.

It can be observed that the ARCCgram achieves the highest ADF value across all three datasets, indicating that the FCF and its harmonics in its diagnostic spectrum exhibit the greatest prominence relative to the local noise floor. This quantitative result is consistent with the qualitative observations presented in the preceding sections.

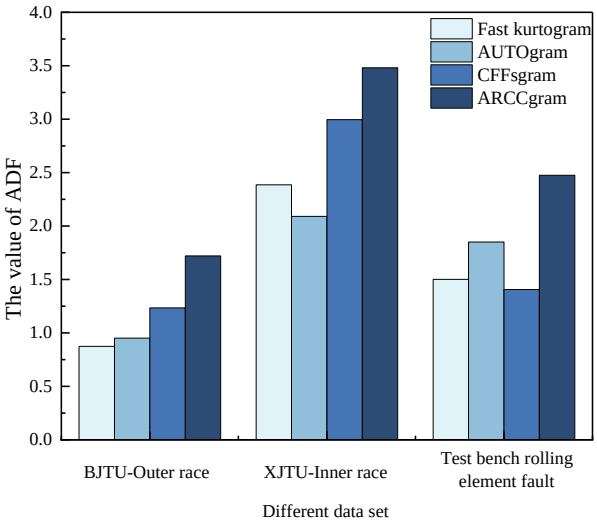


Figure 13. The ADF comparison of different methods for axle-box bearing fault signals.

6. Conclusion

In this study, the ARCCgram is proposed as a novel blind feature extraction method for optimal demodulation band selection in rolling bearing diagnostics. By automatically capturing candidate fault frequencies from the fast spectral coherence map, the formulated ARCC indicator endows blind band evaluation with cyclic-frequency selectivity, eliminating the requirement for prior knowledge of bearing geometry or theoretical fault frequencies. Then, the improved envelope spectrum generated via in-band integration effectively suppresses spurious interference and yields much clearer fault harmonic patterns. The validations on experimental datasets demonstrate that the ARCCgram exhibits high robustness under strong noise and complex interference, reliably outperforming the Fast kurtogram, Autogram, and CFFsgram. Moreover, the advantage of the ARCCgram is quantitatively confirmed by the adjusted diagnostic feature (ADF) values analysis across all test cases.

The results support the effectiveness of the proposed method for the analysed records, while its performance under appreciable PCS broadening requires further validation. When higher order components or sidebands are noticeably broadened, possible extensions include combining evidence from peaks at neighbouring cyclic frequencies, adjusting the windows to the observed broadening, and integrating over the broadened intervals to represent component strength. Future work will investigate these extensions and evaluate the method under varying speed, changing loads and compound fault conditions.

Acknowledgements

The authors are grateful for the financial support provided by the National Natural Science Foundation of China (Grant No.72561016) and the Innovation Fund Project of Lanzhou Jiaotong University and Southwest Jiaotong University (Grant No.LH2024021).

References

1. Wang J, Abdullah S, Arifin A, Karam Singh SS, Gao C. A semi-supervised fault diagnosis method for rolling bearing using time-frequency transform enhanced contrastive learning. *Eksploatacja i Niezawodnosc - Maintenance and Reliability* 2026; 28(1): 207015. https://doi.org/10.17531/ein/207015.
2. Zhu J, Li O, Chen M, Hu B, Ma E. Rolling bearing fault diagnosis method based on adaptive signal diagnosis network and its application. *Eksploatacja i Niezawodnosc – Maintenance and Reliability* 2025; 27(2): 194673. https://doi.org/10.17531/ein/194673.
3. Randall RB, Antoni J. Rolling element bearing diagnostics—A tutorial. *Mechanical Systems and Signal Processing* 2011; 25(2): 485-520. https://doi.org/10.1016/j.ymssp.2010.07.017.
4. Antoni J. Cyclic spectral analysis of rolling-element bearing signals: Facts and fictions. *Journal of Sound and Vibration* 2007; 304(3-5): 497-529. https://doi.org/10.1016/j.jsv.2007.02.029.
5. Chen B, Zhang W, Gu JX, Song D, Cheng Y, Zhou Z, Gu F, Ball AD. Product envelope spectrum optimization-gram: An enhanced envelope analysis for rolling bearing fault diagnosis. *Mechanical Systems and Signal Processing* 2023; 193: 110270. https://doi.org/10.1016/j.ymssp.2023.110270.
6. Randall RB, Antoni J, Chobsaard S. The relationship between spectral correlation and envelope analysis in the diagnostics of bearing faults and other cyclostationary machine signals. *Mechanical Systems and Signal Processing* 2001; 15(5): 945-962. https://doi.org/10.1006/mssp.2001.1415.
7. Wang D, Zhao X, Kou LL, Qin Y, Zhao Y, Tsui KL. A simple and fast guideline for generating enhanced/squared envelope spectra from spectral coherence for bearing fault diagnosis. *Mechanical Systems and Signal Processing* 2019; 122: 754-768. https://doi.org/10.1016/j.ymssp.2018.12.055.
8. Dao PN, Nguyen QP, Vu MH. Adaptive optimal coordination control of perturbed Bilateral Teleoperators with variable time delays using Actor–Critic Reinforcement Learning algorithm. *Mathematics and Computers in Simulation* 2025; 229: 151-175. https://doi.org/10.1016/j.matcom.2024.09.007.
9. Dao PN, Phung MH. Nonlinear robust integral based actor–critic reinforcement learning control for a perturbed three-wheeled mobile robot with mecanum wheels. *Computers and Electrical Engineering* 2025; 121: 109870. https://doi.org/10.1016/j.compeleceng.2024.109870.
10. Dao PN, Nguyen VQ, Duc HAN. Nonlinear RISE based integral reinforcement learning algorithms for perturbed Bilateral Teleoperators with variable time delay. *Neurocomputing* 2024; 605: 128355. https://doi.org/10.1016/j.neucom.2024.128355.
11. Dang NT, Dao PN. Data-driven reinforcement learning control for quadrotor systems. *International Journal of Mechanical Engineering and Robotics Research* 2024; 13(5): 495-501. https://doi.org/10.18178/ijmerr.13.5.495-501.
12. Smith WA, Borghesani P, Ni Q, Wang K, Peng Z. Optimal demodulation-band selection for envelope-based diagnostics: A comparative study of traditional and novel tools. *Mechanical Systems and Signal Processing* 2019; 134: 106303. https://doi.org/10.1016/j.ymssp.2019.106303.
13. Antoni J. Fast computation of the kurtogram for the detection of transient faults. *Mechanical Systems and Signal Processing* 2007; 21(1): 108-124. https://doi.org/10.1016/j.ymssp.2005.12.002.

14. Borghesani P, Smith WA, Randall RB, Antoni J, El Badaoui M, Peng Z. Bearing signal models and their effect on bearing diagnostics. *Mechanical Systems and Signal Processing* 2022; 174: 109077. https://doi.org/10.1016/j.ymssp.2022.109077.
15. Antoni J. The infogram: Entropic evidence of the signature of repetitive transients. *Mechanical Systems and Signal Processing* 2016; 74: 73-94. https://doi.org/10.1016/j.ymssp.2015.04.034.
16. Moshrefzadeh A, Fasana A. The Autogram: An effective approach for selecting the optimal demodulation band in rolling element bearings diagnosis. *Mechanical Systems and Signal Processing* 2018; 105: 294-318. https://doi.org/10.1016/j.ymssp.2017.12.009.
17. Miao Y, Zhao M, Lin J. Identification of mechanical compound-fault based on the improved parameter-adaptive variational mode decomposition. *ISA Transactions* 2019; 84: 82-95. https://doi.org/10.1016/j.isatra.2018.10.008.
18. Hebda-Sobkowicz J, Zimroz R, Pitera M, Wyłomańska A. Informative frequency band selection in the presence of non-Gaussian noise – a novel approach based on the conditional variance statistic with application to bearing fault diagnosis. *Mechanical Systems and Signal Processing* 2020; 145: 106971. https://doi.org/10.1016/j.ymssp.2020.106971.
19. Chen X, Guo Y, Na J. Improvement on IESFOgram for demodulation band determination in the rolling element bearings diagnosis. *Mechanical Systems and Signal Processing* 2022; 168: 108683. https://doi.org/10.1016/j.ymssp.2021.108683.
20. Borghesani P, Pennacchi P, Chatterton S. The relationship between kurtosis- and envelope-based indexes for the diagnostic of rolling element bearings. *Mechanical Systems and Signal Processing* 2014; 43(1-2): 25-43. https://doi.org/10.1016/j.ymssp.2013.10.007.
21. Liu C, He C, Han T, Sun H, Hu S, Shi X. Low-variance version of the RCC index and form factor index for machine condition monitoring. *Mechanical Systems and Signal Processing* 2023; 200: 110614. https://doi.org/10.1016/j.ymssp.2023.110614.
22. Mo Z, Zhang H, Shen Y, Wang J, Fu H, Miao Q. Conditional empirical wavelet transform with modified ratio of cyclic content for bearing fault diagnosis. *ISA Transactions* 2023; 133: 597-611. https://doi.org/10.1016/j.isatra.2022.06.027.
23. Borghesani P, Shahriar MR. Cyclostationary analysis with logarithmic variance stabilisation. *Mechanical Systems and Signal Processing* 2016; 70-71: 51-72. https://doi.org/10.1016/j.ymssp.2015.08.014.
24. Borghesani P, Antoni J. CS2 analysis in presence of non-Gaussian background noise – Effect on traditional estimators and resilience of log-envelope indicators. *Mechanical Systems and Signal Processing* 2017; 90: 378-398. https://doi.org/10.1016/j.ymssp.2016.12.033.
25. Cheng Y, Wang S, Chen B, Mei G, Zhang W, Peng H, Tian G. An improved envelope spectrum via candidate fault frequency optimization-gram for bearing fault diagnosis. *Journal of Sound and Vibration* 2022; 523: 116746. https://doi.org/10.1016/j.jsv.2022.116746.
26. Chen B, Cheng Y, Allen P, Wang S, Gu F, Zhang W, Ball AD. A product envelope spectrum generated from spectral correlation/coherence for railway axle-box bearing fault diagnosis. *Mechanical Systems and Signal Processing* 2025; 225: 112262. https://doi.org/10.1016/j.ymssp.2024.112262.
27. Antoni J, Xin G, Hamzaoui N. Fast computation of the spectral correlation. *Mechanical Systems and Signal Processing* 2017; 92: 248-277. https://doi.org/10.1016/j.ymssp.2017.01.011.
28. Smith WA, Fan Z, Peng Z, Li H, Randall RB. Optimised Spectral Kurtosis for bearing diagnostics under electromagnetic interference. *Mechanical Systems and Signal Processing* 2016; 75: 371-394. https://doi.org/10.1016/j.ymssp.2015.12.034.
29. Smith WA, Borghesani P, Randall RB, Antoni J, El Badaoui M, Peng Z. High-speed bearing diagnostics: Observations from the Surveillance 8 Safran contest data. *Mechanical Systems and Signal Processing* 2024; 216: 111484. https://doi.org/10.1016/j.ymssp.2024.111484.
30. Zhou N, Cheng Y, Wang Z, Chen B, Zhang W. CFFsgram: A candidate fault frequencies-based optimal demodulation band selection method for axle-box bearing fault diagnosis. *Measurement* 2023; 207: 112368. https://doi.org/10.1016/j.measurement.2022.112368.